A computational investigation of electrotonic coupling between pyramidal cells in the cortex

Jennifer Crodelle [1*], Douglas Zhou [2*], Gregor Kovačič [3], David Cai [2, 4, †]

September 25, 2020

[1]*jcrodelle@middlebury.edu
[2]*zdz@sjtu.edu.cn

Abstract

The existence of electrical communication among pyramidal cells (PCs) in the adult cortex has been debated by neuroscientists for several decades. Gap junctions (GJs) among cortical interneurons have been well documented experimentally and their functional roles have been proposed by both computational neuroscientists and experimentalists alike. Experimental evidence for similar junctions among pyramidal cells in the cortex, however, has remained elusive due to the apparent rarity of these couplings among neurons. In this work, we develop a neuronal network model that includes observed probabilities and strengths of electrotonic coupling between PCs and gap-junction coupling among interneurons, in addition to realistic synaptic connectivity among both populations. We use this network model to investigate the effect of electrotonic coupling between PCs on network behavior with the goal of theoretically addressing this controversy of existence and purpose of electrotonically-coupled PCs in the cortex.

Introduction

Electrical communication between pyramidal cells (PCs) in the mammalian cortex has been of interest to neuroscientists for many years. During the early stages of development, PCs are coupled by electrical junctions (EJs) with decreasing degrees of connectivity over the first few postnatal weeks [19, 32]. Experiments have shown that blocking these junctions during embryonic stages of development disrupts the final placement of neurons in the adult cortex, suggesting a role for EJs during development in neuron migration. These experiments on development in rodents report no EJs present in the cortex past the first postnatal week; however, two experimental labs have recently measured the properties of EJs between PCs in the adult cortex [17,31]. Mercer et al. [17] discovered one pair of EJ-coupled PCs in the rat neocortex, while Wang et al. [31] measured ten EJ-coupled pairs of PCs in the prefrontal and visual cortices of rats and ferrets. The protein that might form this electrotonic connection remains unknown, making further experimental investigation difficult [31]. Additionally, the coupling strength of EJs in the adult brain is much higher than the strength measured in the developing cortex, 50% transmission in adults compared to 7% in the first postnatal week, indicating that these might not be the same junctions. Due to the inability of many experimental labs to detect these rare EJs among PCs in the adult cortex, neuroscientists are not yet completely convinced of their existence [18], leading to a controversy over any potential functional role.

Gap junctions (GJs), electrical connections that typically form between the dendrites of inhibitory neurons, on the other hand, have been well studied [10–12]. GJs between a particular type of inhibitory cell called fast-spiking (FS) cells are ubiquitous in the cortex, both in the adult and during development, and have been suggested to promote synchronous and oscillatory activity among neurons in the cortex [1,4,12,24,26]. In particular, GJs between FS cells are typically comprised of the channel protein Connexin-36 and several knock-out experiments have been performed to deduce their function in promoting synchrony and oscillations. Since the protein that makes up the junction between PCs has not yet been discovered, we follow the terminology in the study by Wang et al. [31] and refer to the junction between PCs as an electrotonic junction (EJ) and the one between FS cells as a gap junction (GJ) to easily distinguish between the junctions that couple the two different types of neurons. In this work, we address the controversy over the existence of EJs between PCs by

---

[1]Middlebury College
[2]Shanghai Jiao Tong Univeristy

using a computational model to investigate their potential functional role in altering the dynamics of a network containing both ubiquitous GJ coupling, as well as rare, pair-wise EJ coupling.

We show that the global network behavior is largely unaffected by the addition of pair-wise EJ coupling when synaptic connections are sparse and random, offering one possible conclusion to the controversy: that the presence or absence of EJ-coupled PCs does little to influence network behavior. On the other hand, we also show that the EJ-coupled PCs themselves exhibit pair-wise synchrony and oscillations generated through fast mutual excitation. The influence of this pair-wise synchrony on network activity, however, is barely discernible from network fluctuations. Next, we consider a network containing strengthened synaptic connections from EJ-coupled PCs to GJ-coupled FS cells. We show that the presence of EJ coupling between such pairs of PCs can serve to reduce noise in incoming signals and elicit network activity with highly variable firing patterns, suggesting a possible functional role in information processing.

The paper is organized as follows. In the Methods section, we describe the neuron models, a measure for determining the magnitude of synchrony, and the parameter set for FS cells and PCs in our model. In the Results section, we construct a realistic cortical network model, with sparse synaptic coupling and ubiquitous GJ-coupling among FS cells, and

characterize properties of the network dynamics for multiple network dynamical regimes, in the presence and absence of both GJ coupling among FS cells and pair-wise EJ coupling between PCs.

Methods

Cortical neuron model

In this work, we use the Hodgkin-Huxley (HH) equations to describe the membrane potential of each cell in the model network. While other point-neuron models use modified versions of the simpler integrate-and-fire (IAF) model to account for the weak GJ coupling among interneurons [6, 15, 20], the experimentally-measured properties of a strong EJ between pyramidal cells cannot be well-captured by an IAF model. Specifically, due to the strong conductance of the EJ, the post-junctional voltage is sensitive to changes in the pre-junctional voltage, especially during an action potential, resulting in the shape and size of the post-junctional spikelet being dependent on the shape and size of the pre-junctional action potential [31].

The HH model utilized in this work is described as follows. The voltage v_i across the cell membrane of the ith neuron with capacitance C is described by the set of equations

$$C\frac{dv_i}{dt} = -g_L(v_i - v_R) - \bar{g}_{Na}m^3h(v_i - v_{Na}) - \bar{g}_K n^4(v_i - v_K) - g_C\sum_j(v_i - v_j) - G_i^Q(t)(v_i - v^Q), \qquad (1)$$

where the synaptic conductances, $G_i^Q(t)$, are described by the equations

$$\frac{d}{dt}G_i^Q(t) = -\frac{G_i^Q(t)}{\sigma_r} + G_{i,\ell}^Q(t), \qquad \frac{d}{dt}G_{i,\ell}^Q(t) = -\frac{G_{i,\ell}^Q(t)}{\sigma_r} + G_{i,\ell+1}^Q(t), \qquad \ell = 1, 2, 3$$

$$\frac{d}{dt}G_{i,4}^Q(t) = -\frac{G_{i,4}^Q(t)}{\sigma_r} + \sum_{j\neq i}S_{ij}^Q g(v_j^{\mathrm{pre}}) + \sum_k f^Q\delta(t - T_i^k), \qquad Q = \{E, I\}. \qquad (2)$$

In Eq. (1), g_L is the leak conductance, v_R is the resting potential, $\bar{g}_{Na}$ and $\bar{g}_K$ are the maximal sodium and potassium conductances, and v_{Na} and v_K are the sodium and potassium reversal potentials, respectively. The fourth term on the right-hand side describes the current through the electrical junction from all neurons that are coupled to neuron i, influencing the voltage of the ith neuron with conductance strength g_C. The activation and inactivation parameters, m, h, and n, model the gating of the ion channels

and exhibit dynamics described by the equation

$$\frac{dx}{dt} = \alpha_x(v)(1 - x) - \beta_x(v)x, \qquad x = \{m, n, h\},$$

with each rate variable described by the set of

voltage-dependent functions

$$\alpha_m(v) = \frac{-0.32(v - v_T - 13)}{\exp[-(v - v_T - 13)/4] - 1},$$

$$\beta_m(v) = \frac{0.28(v - v_T - 40)}{\exp[(v - v_T - 40)/5] - 1},$$

$$\alpha_h(v) = 0.128 \exp[-(v - v_T - 17)/18],$$

$$\beta_h(v) = \frac{4}{1 + \exp[-(v - v_T - 40)/5]},$$

$$\alpha_n(v) = \frac{-0.032(v - v_T - 15)}{\exp[-(v - v_T - 15)/5] - 1},$$

$$\beta_n(v) = 0.5 \exp[-(v - v_T - 10)/40],$$

as determined by Pospischil et al. [22] for FS interneurons and PCs in the mammalian cortex.

The final term in Eq. (1) describes the current received by the ith neuron through excitatory ($Q = E$) and inhibitory ($Q = I$) synapses. These synaptic conductances are described in Eq. (2) using fourth-order kinetics as in Ref. [25]. The input from the jth presynaptic cell is filtered through the function

$$g(v) = \frac{1}{1 + \exp(-(v - 20)/2)}.$$

The right-hand side of the dynamical equation for $G_{i,4}^Q$ in Eq. (2) contains two sums: The first sum models input from the jth presynaptic neuron with strength S_{ij}^Q for both excitatory and inhibitory synaptic inputs. The second sum models incoming spikes at times T_i^k with strength f^Q that originate from outside the model network. These external spikes are modeled by a Poisson spike train with rate ν. Note that several of the parameters used in this model are chosen through matching of voltage-clamp experimental data for EJ-coupled PCs [31] and GJ-coupled FS cells [10]; see Appendix for details.

Upstream input neuron model

To investigate the dynamical effects of the EJ-coupled PC pairs, we simulate sensory input to PC pairs using the computationally-efficient IAF model, which can capture sufficiently rich network dynamics of neuronal systems. The dynamics of the ith model neuron in the IAF input network are described by the set of

Table 1: Hodgkin-Huxley neuron parameter values used in all simulations, unless otherwise stated.

Parameter	FS cells	PCs
From Literature [22]:		
Capacitance C (μF/cm^2)	1	1
v_R (mV)	-70	-70
v_{Na} (mV)	30	55
v_K (mV)	-90	-80
v^E (mV)	0	0
v^I (mV)	-80	-80
Through matching (see Appendix):		
g_L (mS/cm^2)	0.1	0.025
g_C (mS/cm^2)	0.012	0.08
$\bar{g}_{Na}$ (mS/cm^2)	30	60
$\bar{g}_K$ (mS/cm^2)	5.0	3.0
v_T (mV)	-58	-45

equations

$$C\frac{dv_i}{dt} = -g_L(v_i - \epsilon_R) - g_i^E(t)(v_i - \epsilon^E)$$
$$- g_i^I(t)(v_i - \epsilon^I),$$

$$\sigma^Q\frac{dg_i^Q}{dt} = -g_i^Q + h_i^Q, \qquad Q = \{E, I\},$$

$$\sigma^Q\frac{dh_i^Q}{dt} = -h_i^Q + \sum_{j \neq i} S_j^Q \sum_k \delta\left(t - T_j^k\right)$$
$$+ f^Q \sum_k \delta\left(t - T_i^k\right),$$

where $v_i(t)$ is the voltage of the ith neuron, $C = 1$ μF/cm^2 is the capacitance, g_L is the leak conductance, ϵ_R is the resting potential, and ϵ^E and ϵ^I are the reversal potentials for the excitatory and inhibitory currents, respectively. The synaptic conductance has time constants σ^E and σ^I and synaptic strengths S^E and S^I for excitatory and inhibitory inputs respectively. See Table 2 for parameter values.

The dynamics of the voltage are such that the incoming spikes from other neurons in the network and inputs from the Poisson spike train modulate the voltage. Note that the rate, ν, of the Poisson drive is varied such that the network exhibits a variety of behaviors, but the product $f^Q\nu$ remains constant. In the absence of incoming spikes, the voltage decays exponentially toward the resting potential, ϵ_R. If the voltage is raised such that it reaches a threshold, determined by $v_T = -55$ mV, the neuron is said to have

spiked, the spike time is recorded, and the voltage is reset to ϵ_R. The procedure for efficiently implementing the time-evolution equations and calculating the spike time can be found in Ref. [23]. The IAF model network is all-to-all connected, including 75% excitatory and 25% inhibitory neurons. Results were obtained from simulations of five seconds for each trial.

Table 2: Upstream IAF neuron parameter values used in the structured network, unless otherwise stated.

Parameter	Value	Parameter	Value
g_L (mS/cm^2)	0.05	ϵ_R (mV)	-70
ϵ^E (mV)	0	ϵ^I (mV)	-8
σ^E (ms)	1.0	σ^I (ms)	4.0
S^E (mS/cm^2)	0.2	S^I (mS/cm^2)	0.4
External Drive Parameter		Range	
ν (Hz)		$1000 \to 5000$	
f^E (mS/cm^2)		$11.6 \to 12.1$	
f^I (mS/cm^2)		$10.0 \to 9.2$	

Network Setup

We construct a network of PCs and FS cells with the goal of understanding how EJ-coupling between pairs of PCs affects network dynamics. We organize 400 neurons on a 20×20 grid, including 25% FS cells and 75% PCs [2,5], with the coupling probability from one cell to another, P^Q, dependent on their cell type, where $Q = \{E, I\}$. This probability decays exponentially with distance [16, 33, 34] according to the formula

$$P^Q(x,y) = P^Q \exp\left[-\frac{(\sqrt{x^2+y^2}-1)^2}{8}\right],$$

where x is the horizontal, and y the vertical, distance. Galarreta and Hestrin [10] measured that FS cells form GJ coupling with other FS cells at distances of up to 80 μm with a coupling probability of about 60%. Due to the small size of our network, we allow the FS cells to form a GJ connection with any other FS cell in the network with a coupling probability of 60%. Wang et al. [31] measured that an EJ occurs with a 5% probability between touching or overlapping PCs in the neocortex. In our model, we allow only neighboring (up, down, left, right) PCs to form an EJ with a 5% probability, resulting in pairs of EJ-coupled PCs. Table 3 summarizes the synaptic and electric coupling probabilities used in the cortical network.

Table 3: Table of network connectivity values for the cortical network.

Synaptic coupling parameters	FS cells	PCs
Coupling Probability, P^E (%) (from excitatory neurons)	25	30
Coupling Probability, P^I (%) (from inhibitory neurons)	50	20
Synaptic time constant, σ_r^E (ms) (excitatory)	0.4	0.4
Synaptic time constant, σ_r^I (ms) (inhibitory)	1.0	1.0
Electrical coupling parameters	FS cells	PCs
Coupling Probability (%)	60	5

Synchrony Measure

We developed the SD measure to determine the degree of synchrony within a network synchronous event (NSE) [8]. The NSE is determined by calculating the time at which the average voltage of the network crosses a threshold, indicating a time at which the majority of the population is active within a small window. For each NSE, the time difference from each network spike within ± 20 ms of the NSE time is calculated, counted, and binned. The SD measure is defined as the standard deviation of the distribution of time differences computed for all NSEs in the network. Small values of the SD measure indicate small deviations in the time difference from the NSE time to each spike time of all participating neurons (tight synchrony), whereas larger values of the SD measure indicate larger variations in the time from each neuron's spike time to the NSE time.

Results

The results are organized as follows. First, we consider a network model to investigate the dynamics resulting from the inclusion of EJ and GJ coupling for both mean-dominated and fluctuation-dominated regimes. We show that the inclusion of GJ coupling between FS cells has a strong synchronizing effect on the network, with and without the inclusion of EJ coupling between PCs. In the presence or absence of GJ coupling, adding EJ coupling between a rare number of pairs of PCs has little effect on network synchrony, the observed changes are small and on the order of network fluctuations. Finally, we highlight the pathway from the EJ-coupled PCs to the GJ-coupled FS-cell network and propose a new network structure

4

in which EJ-coupled pairs of PCs might play a role in information processing.

Mean-dominated Regime

We begin with the mean-dominated regime in which the external drive, as described by the frequency of the Poisson spike train, ν, and the strength of each spike, f^Q, has a high frequency and a small strength. Since each neuron receives many spikes, the input to all neurons is nearly uniform, leading to a network of neurons that fire regularly and often synchronously.

We demonstrate that a typical mean-dominated network exhibits regular dynamics through raster plots, a plot of the spike times of all neurons, and inter-spike interval (ISI) histograms, a plot of the time difference between successive spikes for each neuron in the network, for each coupling regime (e.g., EJ coupling); see Fig. 1. First, notice that the networks without GJ coupling (with and without EJ coupling), and similarly the networks with GJ coupling (with and without EJ coupling), have very similar average time differences. We calculate the coefficient of variation (CV), or the ratio of the standard deviation to the mean of the ISI distribution, which describes the regularity of firing patterns of neurons in the network, where a CV value of 1 indicates a Poisson process. Then, CV values less (more) than one indicate a firing pattern more (less) regular than a Poisson process. In the mean-dominated case, all CV values are well below one, indicating regular firing patterns, as expected and demonstrated by the raster plots and ISI plots of Fig. 1.

Note that the ISI distribution may not be a direct indicator of network synchrony since it describes the time difference of successive spikes of each individual neuron, not taking into account the spike timing of other neurons in the network. This means that the firings of two neurons can share an ISI distribution, but not align in time, indicating that they are both firing very regularly and at a similar frequency, but may be unsynchronized. The raster plots, however, show that both networks containing GJ coupling exhibit clear synchrony, as shown by the alignment in time of excitatory (red) and inhibitory (blue) neurons' spike times, while networks that do not contain GJ coupling do not exhibit as clear a synchrony; see Fig. 1.

To aid in our goal of understanding how network dynamics are affected by the addition of EJ coupling, we focus on the oscillations present in networks containing GJ coupling. To quantify characteristics of the oscillations, we calculate properties of the power spectral density (PSD), a measure that determines the power of each frequency present in the network. Specifically, characteristics of the PSD include: the frequency at which the highest peak occurs (most prominent frequency exhibited by the network) and the width and height of this peak (tightness and power of this frequency). Figure 2A shows the average PSD for each coupling regime over 30 realizations. Notice that the networks without GJ coupling do not exhibit strong oscillations, i.e., there is no significant peak in the PSD, as was anticipated from the raster plots in Fig. 1. For this reason, we only focus on the networks with GJ coupling and investigate the difference in frequency, width, and height of the prominent peak of the PSD between cases with or without EJ coupling in the networks; see dashed green and solid purple curves in Fig. 2A.

Notice that the PSD for the networks with or without EJ coupling are very similar. The prominent frequency occurs near 30 Hz in both networks, and the power (height) of the peak corresponding to this frequency, as well as the tightness (width) of this peak, are also very close; see Fig. 2B. To show that this is not the result of the choice in external drive, we vary the rate of external drive, ν, from 4000 to 8000 Hz, where the strengths f^E and f^I are changed for each rate such that $f^Q\nu$ remains constant. Figure 2C shows the percent change from the network without EJ coupling to the network with EJ coupling (i.e., taking the percent change that results from the addition of EJ coupling). Observe that the total changes in all three PSD characteristics are less than 7% for all external rates, indicating that adding EJ coupling to a network that contains GJ coupling does not strongly influence the frequency or power of the oscillations in the network.

Another important characteristic of mean-dominated networks is that the neurons often exhibit synchronous firing. We analyze the synchrony of the different regimes by calculating the number of network synchronous events (NSEs) per second, a measure for network synchrony, and the SD measure, which determines the tightness of each individual NSE (see the Methods section). As shown in the raster plots of Fig. 1, the networks containing GJ coupling behave differently than those that do not. Therefore, to study the synchronous events occurring in each network, we choose two different thresholds for the average voltage; see Fig. 3A. Additionally, since we are interested in determining the effect of adding EJ coupling to a network, it is sufficient to keep the threshold constant for the two network regimes containing GJ coupling, as well as for the two network regimes that do not contain GJ coupling, and measure how the network synchrony properties
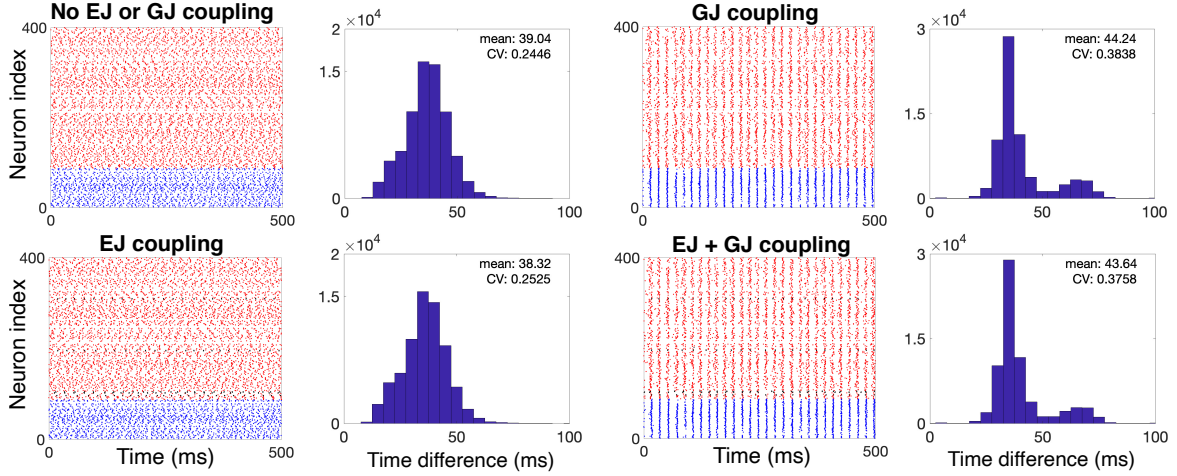
Figure 1: Raster plots and inter-spike interval (ISI) histograms for each of the four coupling regimes: No EJ or GJ coupling, GJ Coupling (but no EJ coupling), EJ Coupling (but no GJ coupling), and both EJ and GJ coupling. Each network receives mean-dominated external input. Parameters are as follows: $\nu = 8000$ Hz, $f^E = 0.23125$ mS/cm^2, $f^I = 0.4$ mS/cm^2, simulation in each trial runs for 10 seconds of simulated time.
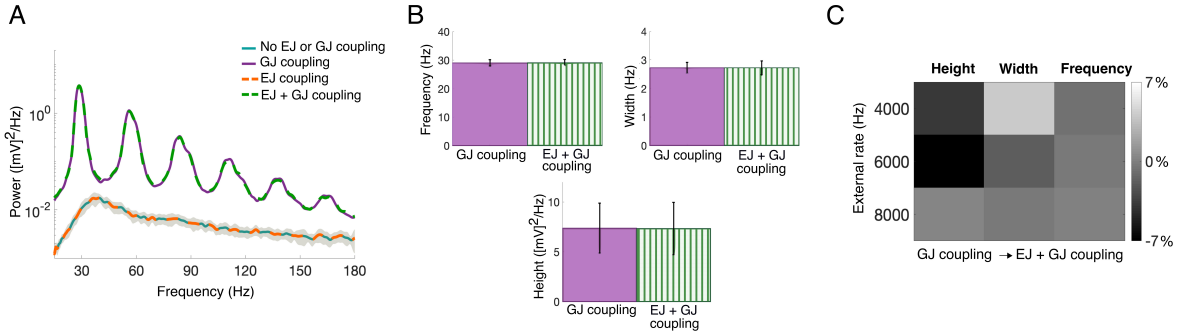

Figure 2: Characteristics of oscillations in the mean-dominated regime. **A**: The power spectral density (PSD) of the network for each coupling case. **B**: Characteristics of the primary peak of the PSD for the network containing GJ coupling comparing the cases with and without EJ coupling. The measurements are averaged over 30 trials, where the error bars represent the standard deviation across the trials. **C**: The difference in height, width, and frequency of the primary peak in the PSD for several values of the external rate, ν, calculated as a percent change between GJ-coupled networks with and without EJ coupling. The external drive parameters for the network shown in **A** and **B** are: $\nu = 8000$ Hz, $f^E = 0.231$ mS/cm^2, $f^I = 0.4$ mS/cm^2. As the external rate ν changes in **C**, the strengths change such that $f^E\nu$ and $f^I\nu$ remain constant at 1850 mS/(s $\cdot$ cm^2) and 3200 mS/(s $\cdot$ cm^2), respectively.

change with the addition of EJ coupling. First, notice that the number of NSEs per second and the SD measure do not change significantly with the addition of EJ coupling, as shown in Figs. 3B and C. Note that while the number of NSEs per second in the networks that do not contain GJ coupling (solid blue and striped orange bars) is higher than for the networks containing GJ coupling (striped green and solid purple bars), the SD measure shows that those events are more tightly synchronized for the networks containing GJ coupling, as expected from the average voltage plots in Fig. 3A. The tightness of each NSE, as well as the number of NSEs, does not significantly change with the addition of EJ coupling, as shown in Fig. 3D by calculating the percent change of each network with the addition of EJ coupling over many values of the external rate.

The addition of EJ coupling in the presence of a mean-dominated external drive does not seem to significantly impact the oscillatory or synchronous network dynamics. We next consider a network in which the external drive is fluctuation-dominated and measure changes in network properties with the addition of EJ coupling.

Fluctuation-dominated regime

In this section, we examine the fluctuation-dominated regime and characterize changes in the network behavior as a function of the addition of EJ coupling. First, we point out that the dynamics of networks receiving fluctuation-dominated input differs from those receiving mean-dominated input; see Fig. 4. In particular, networks receiving fluctuation-dominated input do not exhibit oscillations, and even the networks containing GJ coupling do not exhibit much synchrony. The ISI distributions are broad, with CV values greater than one, indicating that the networks are firing irregularly. Note that the difference in the CV value for the networks with GJ coupling, with and without EJ coupling, is larger than those in the mean-dominated case.

Therefore, we characterize changes induced by the addition of EJ coupling by looking at the ISI and CV over many realizations in Figs. 5A and B, and several values of the external rate in Fig. 5C. Notice that the networks containing GJ coupling have, on average, lower ISI values and higher CV values than those without GJ coupling (with or without EJ coupling), indicating that the neurons in these networks fire closer together in time and more irregularly. However, adding EJ coupling to the network that does not contain GJ coupling seems to have negligible effects on the CV, see striped orange and solid

blue bars in Fig. 5B and the two left-most columns of the ISI and CV portions of Fig. 5C. The CV values do change with the addition of EJ coupling to a GJ-coupled network; however, these values are small, at most we see a percent of change of around 6%, and the effect (either an increase or decrease in CV value) seems to vary with changes in the external rate, note the light and dark squares in the final column of Fig. 5C. Note that these changes exemplify the stochasticity of the model and further emphasize the lack of significant evidence for a discernible effect that the addition of EJ coupling might have on global network properties.

Though the network effects resulting from the addition of EJ coupling are small, we expect that the EJ itself strongly couples pairs of PCs. Therefore, we next analyze the behavior of these pairs of PCs within each network regime and characterize how the dynamics of the PCs themselves are affected by the addition of an EJ.

EJ pairs of PCs

In this section, we characterize the behavior of the pairs of PCs in each coupling regime receiving different types of external drive. We begin by showing that the EJ-coupled pairs of PCs are strongly synchronized when compared to those same pairs without EJ coupling; see raster plots of a few example pairs of EJ-coupled PCs in Fig. 6A. We use the van Rossum distance, a measure for determining the degree of synchrony between the spike trains of two neurons [30], to quantify this synchrony by calculating the distance between the spike trains of each EJ-coupled pair and averaging over all EJ-coupled pairs for each network coupling regime. It is clear that the network regimes in which the PCs contain EJ coupling (with and without GJ coupling) have a much smaller van Rossum distance than those without EJ coupling; see orange and green striped bars as compared to blue and purple solid bars in Fig. 6B. We also observe that the addition of GJ coupling to the network creates a smaller van Rossum distance between the pairs that are not EJ coupled simply because the inhibition from the GJ-coupled interneurons creates more regular firing of all neurons in the network; compare the blue and purple solid bars in Fig. 6B. Interestingly, the van Rossum distance of the EJ-coupled cells in a network without GJ coupling is much lower than the network containing both EJ and GJ coupling, see orange compared to green striped bars. This implies that the EJ tightly synchronizes the two pyramidal cells, but that this synchrony can be influenced by the behavior of the other neurons in the network, such as the GJ-
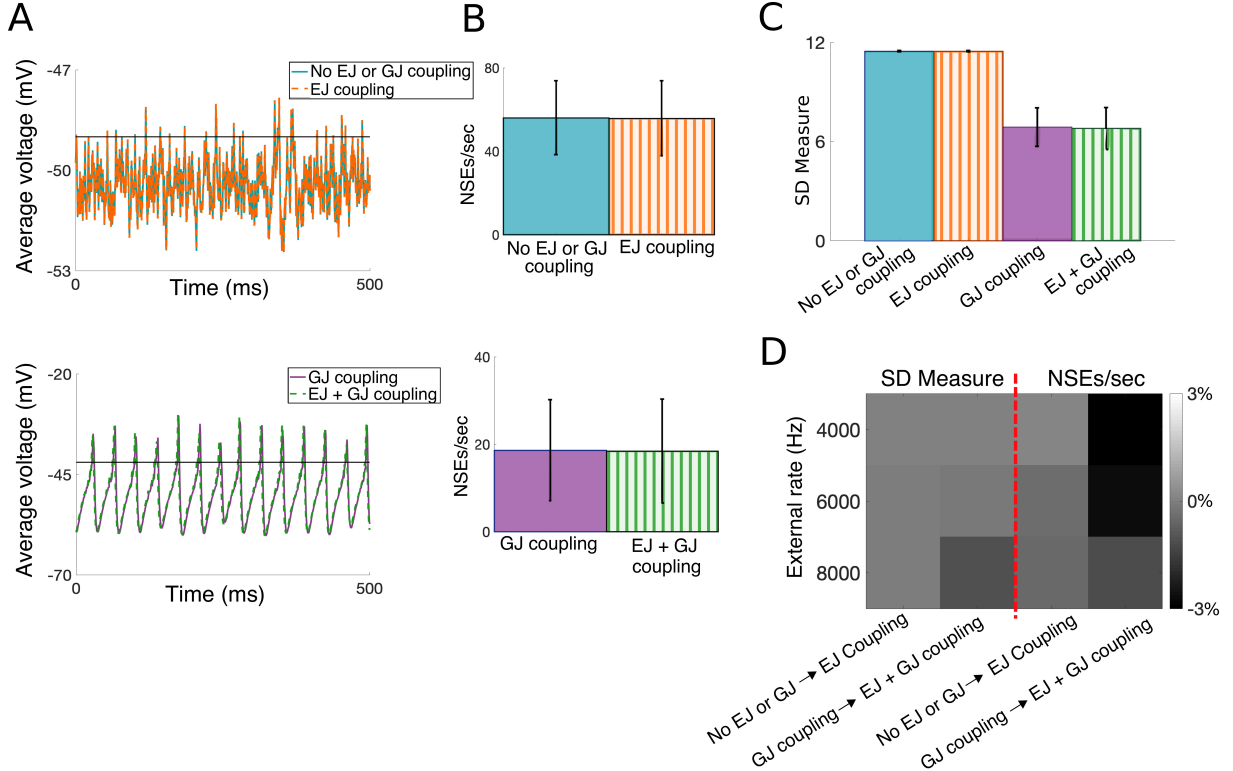
Figure 3: Synchrony measures for networks receiving a mean-dominated external drive. **A**: The average voltage of all neurons in the network, excluding the EJ-coupled cells, for the non-GJ-coupled networks with or without EJ coupling (top), and the GJ-coupled networks with or without EJ coupling (bottom). The threshold for determining NSEs are shown as black lines at -49 mV and -42 mV, respectively. **B**: The number of NSEs per second for each regime, where the black bars indicate standard deviation over 30 realizations and the colors coordinate with the regime described in **A**, and are labeled below each bar. **C**: The SD measure for each network regime. The networks shown in **A**-**C** are for $\nu = 8000$ Hz,$f^E = 0.231$ mS/cm^2, $f^I = 0.4$ mS/cm^2. **D**: The percent of change in the number of NSEs per second and the SD measure from network without EJ coupling (with and without GJ coupling) to the network containing EJ coupling (with and without GJ coupling).

coupled interneurons.

We next look at the van Rossum measure over different values of the external drive. Observe that the distance between the spike trains of EJ-coupled PCs in both a network with just EJ coupling and a network containing both EJ and GJ coupling decreases with an increase in the external rate; see Fig. 6C. Interestingly, the van Rossum distance between PC pairs in a network containing GJ coupling changes more drastically over the external drive than in networks without it, reinforcing the idea of competition between the network dynamics and the strong EJ coupling between the pair of PCs.

Clearly an EJ between pairs of PCs affects the behavior of those pairs, but we have shown that the resulting change in behavior does not significantly alter the network dynamics. There are, however, subtle

changes in network behavior that can be attributed to the addition of EJ coupling. For example, in the mean-dominated regime, we have shown that there does not seem to be a significant change in the number of NSEs from a network containing GJ coupling to a network containing both EJ and GJ coupling. However, it might be the case that the synchrony between the EJ-coupled PCs is indeed transmitted to the network, but that the result is small. We show in Fig. 7 that there are indeed small changes in the behavior of the network in response to the addition of EJ coupling. For example, we count the number of spikes occurring in the network in an interval of $\pm$ 20 ms from each NSE; see Fig. 7A. The results shown in Fig. 7A indicate that the addition of EJ coupling might elicit more neurons to spike during each NSE. Additionally, we calculate the average voltage
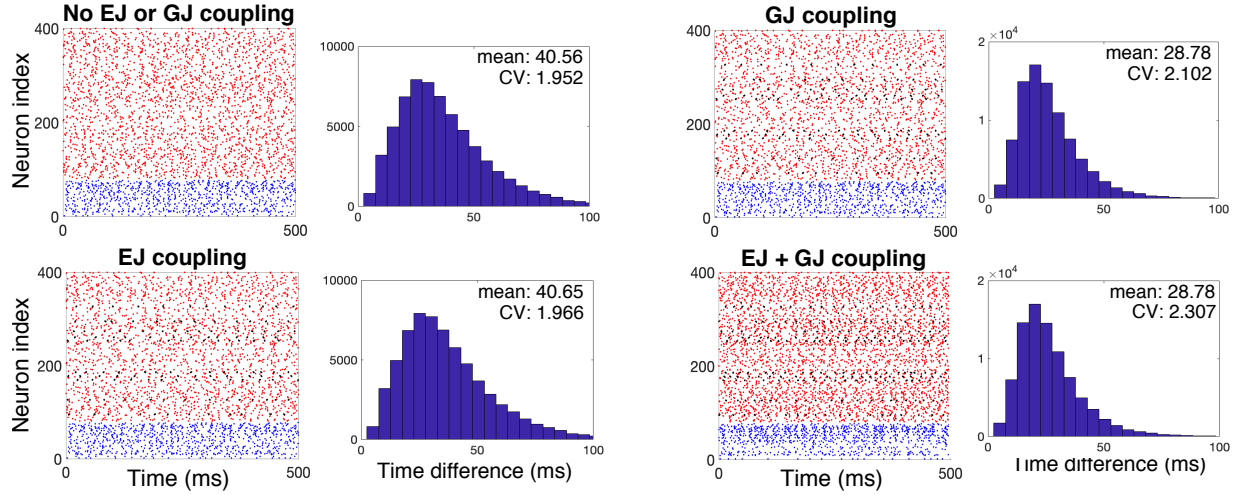
Figure 4: Raster plots and inter-spike interval (ISI) histograms for each network regime receiving fluctuation-dominated external input. Parameters for this figure are as follows: $\nu = 1000$ Hz, $f^E = 1.85$ mS/cm^2, $f^I = 3.2$ mS/cm^2, simulation run for a total of 10 seconds.
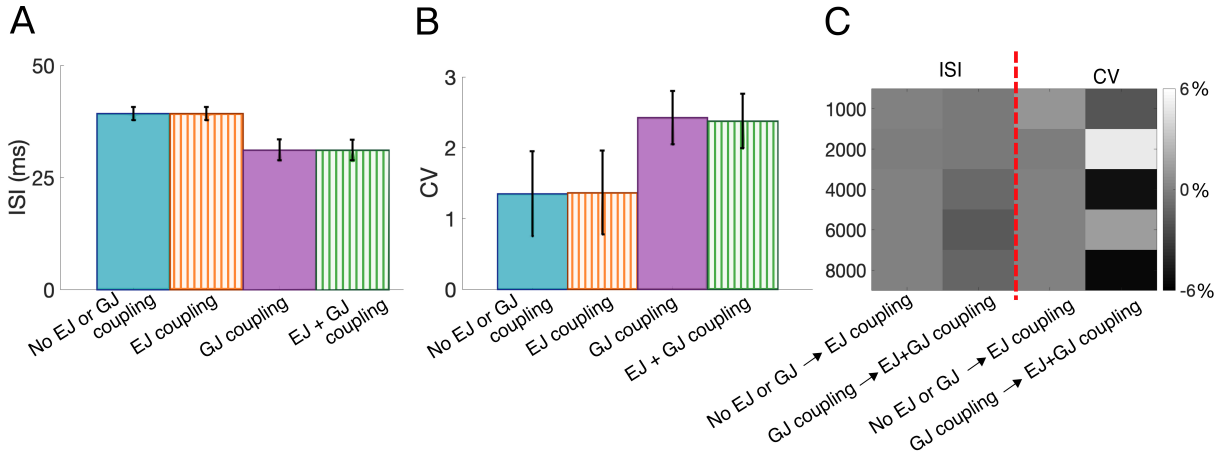

Figure 5: Changes in the ISI and CV in a fluctuation-dominated regime. **A**: The average ISI for each coupling regime, and **B**: the CV for each coupling regime, where black bars indicate standard deviation over 30 realizations. These results are for a fluctuation-dominated network where $\nu = 1000$ Hz, $f^E = 1.85$ mS/cm^2, $f^I = 3.2$ mS/cm^2. **C**: The percent of change from a network without EJ coupling to a network with EJ coupling, for all values of the external rate.
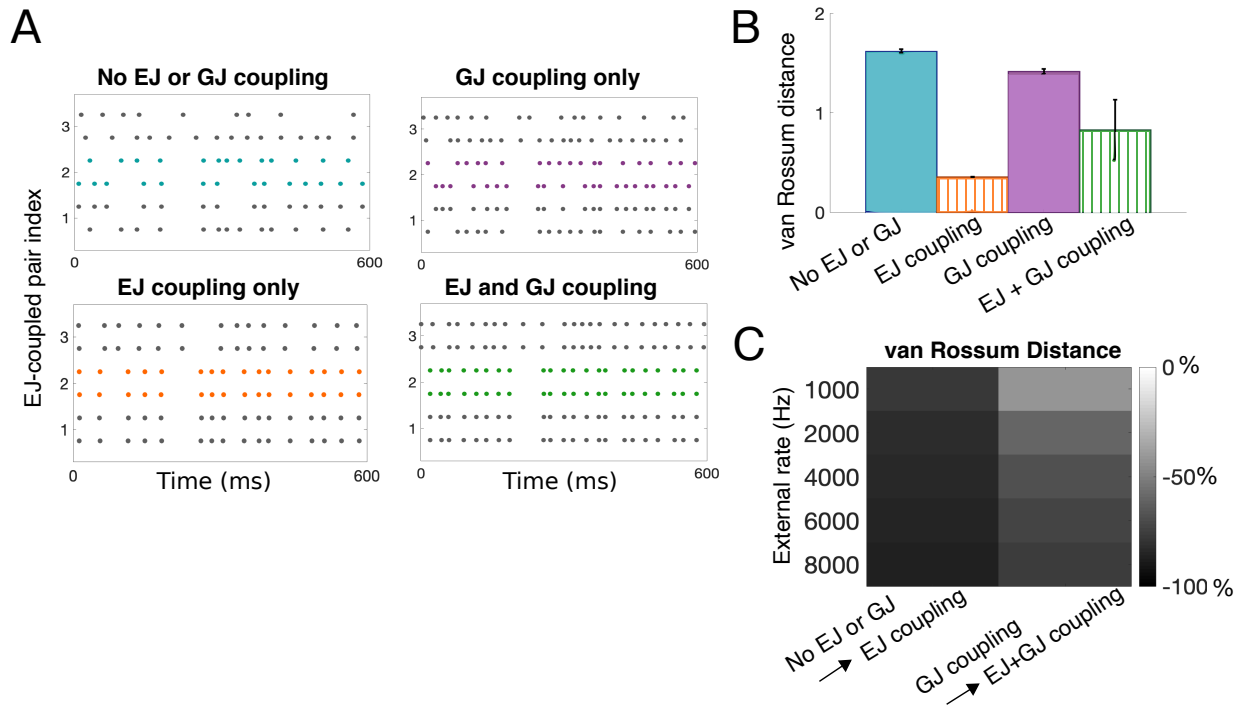
Figure 6: Characteristics of the behavior of EJ-coupled PC pairs. **A**: Raster plots for the spike times of three example EJ-coupled PC pairs in each network regime. Each pair is colored to match the paired cell, with the middle color coordinating with the coupling regime. **B**: The van Rossum distance between the spike trains of each EJ-coupled pair of cells, averaged over all pairs in each network, for the network of $\nu = 1000$ Hz. Black bars indicate standard deviation over 30 realizations. **C**: The percent change in van Rossum distance from networks containing no EJ coupling to those containing EJ coupling (i.e., no EJ or GJ coupling to EJ coupling (but no GJ coupling) and GJ coupling (but no EJ coupling) to both EJ and GJ coupling.)

of all cells in the network (excluding the EJ-coupled PC pairs), subtract out the mean of this curve, and calculate the positive area. This is a measure for the density of coinciding active neurons since higher peaks in the average voltage correspond to synchronized events; see Fig. 7B. The percent of change from a network containing GJ coupling to a network containing both EJ and GJ coupling is positive, as shown in the right column of Fig. 7C, indicating that the density of active neurons during each NSE increases with the addition of EJ coupling.

We have shown in this section that the coupled PC pairs are significantly influenced by the addition of an EJ and that the GJ-coupled interneurons affect the dynamics exhibited by these pairs (recall Fig. 6B). Also, though the effect is small, we have shown that the addition of EJ coupling can lead to an increase in the number of active neurons during synchronous network events (see Fig. 7). In previous sections, we have shown that for several different network regimes, using experimentally-observed synaptic connectivity percentages and weights of the adult neocortex, the behavior of a network without EJ coupling does not differ significantly from one that contains EJ coupling. However, assuming the EJ is present in the network for a purpose, we use the small changes in the behavior of EJ-coupled cells as a basis for a conjecture on a possible network role for EJ-coupled between pairs of PCs.

Possible functional role for EJ-coupled PC pairs

The PCs connected by an EJ exhibit clear synchrony; however, this synchrony does not seem to significantly impact the synchrony of the rest of the network. The observed effects are small, eliciting less than a 5% change in network synchrony with the addition of EJ coupling. One suggestion is that, due to the sparse synaptic coupling of the cortex, the synchronizing effects of the EJ between pairs of PCs do not propagate to the rest of the network. Although cortical synaptic coupling is sparse on average, this does not exclude the possibility that certain synapses are selectively strengthened. Therefore, to uncover a possible functional role for these EJ-coupled pairs of PCs, we design a network in which the synapses that transmit information to and from the EJ-coupled PCs are strengthened.

Specifically, we restrict our focus to the regime in which the network contains GJ coupling, since realistic cortical networks contain GJ coupling, and choose one EJ-coupled PC pair to analyze [deemed the Network-Driven Excitatory Pair (NDEP)]. We

include a ten-fold increase in the synaptic connections from the NDEP to the GJ-coupled inhibitory neurons, and a three-fold increase in the synaptic strength from the inhibitory cells back to the NDEP. Note that the coupling probabilities among the different cell types, P^Q, remain the same as described in Table 3 and we fix the external drive at $\nu = 5000$ Hz and $f^E = 0.2$ mS/cm^2 and $f^I = 0.44$ mS/cm^2. Additionally, we assume a fraction of the population, 20% of the inhibitory cells and 30% of the excitatory cells, receive an additional sensory drive mimicking an incoming sensory stimulus. This drive is modeled by a Poisson spike train with rate $\nu = 100$ Hz, and f^E_{sens} = 3.5 mS/cm^2 and f^I_{sens} = 10.0 mS/cm^2 for those randomly-chosen neurons. The NDEP, however, receives sensory drive from the upstream IAF neurons, so that the spike times received by the NDEP can be controlled to go from unsynchronized to synchronized by controlling the external drive to the upstream IAF network.

In detail, the IAF upstream network is stimulated using external rates in the ranges described in Table 2, where the synchrony of each simulation can be measured by counting the number of times the instantaneous firing rate of the IAF network crosses a threshold (similarly to the process of finding the NSEs), called the input synchrony. Figure 8A shows two example IAF raster plots and the resulting instantaneous firing rates, with the threshold for determining the input synchrony shown as a red line. The NDEP, shown imbedded in the HH model schematic in Fig. 8B, receives the previously-computed spikes from a set of neurons in the IAF model chosen randomly, but consistently, such that each PC in the NDEP receives, on average, the same number of spikes (for all input synchrony values). We analyze the behavior of the neurons in the NDEP and, more importantly, the behavior of the downstream cortical network, as a function of this input synchrony, with a particular focus on potential functional roles the EJ might play in organizing network activity.

Due to the increase in synaptic strength from the NDEP to the interneuron population, we find that spiking of both neurons in the NDEP can elicit network-wide firing events, or NSEs. To illuminate a possible role of the EJ, we measure the number of NSEs that result from the firing of an NDEP that is EJ-coupled (has a conductance value, g_C, of 0.08 mS/cm^2) and the NDEP that has the EJ turned off (conductance is set to zero). We show that a network containing an NDEP with the EJ turned on produces significantly more NSEs than one with the EJ turned off, see the top panel of Fig. 8C. This increase in the number of NSEs is consistent across all input syn-
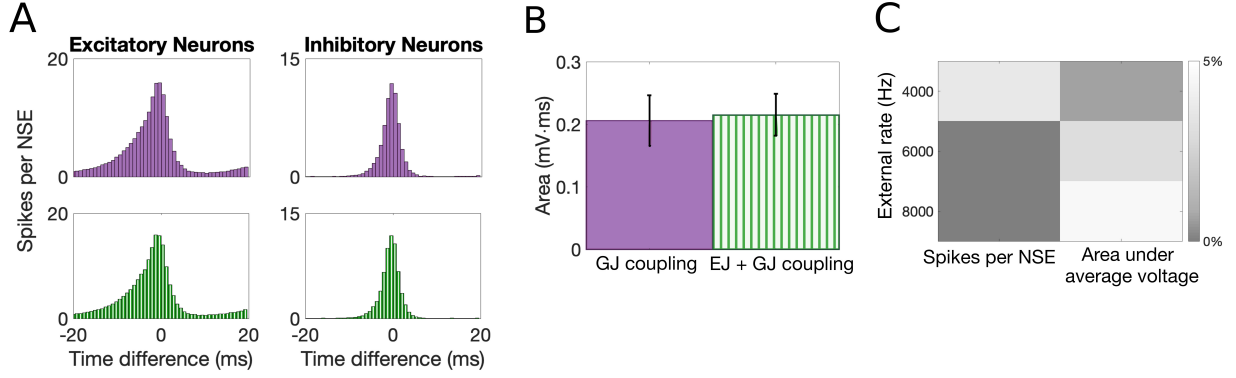
11

Figure 7: EJ-coupled PCs influence network behavior **A**: A histogram of the number of spikes, split to show the excitatory and inhibitory spikes separately, occurring within $\pm$ 20 ms of each NSE, for the network containing GJ coupling only (solid purple) and the network containing both EJ and GJ coupling (striped green). **B**: The area under the average-voltage curve for all neurons in the network, excluding the EJ-coupled pairs, for the network containing GJ coupling (solid purple) and both EJ and GJ coupling (striped green). **C**: The percent of change from a network with just GJ coupling [solid purple in **A** and **B**] to a network containing both EJ and GJ coupling [striped green in **A** and **B**] for the number of spikes per NSE and the area under the average-voltage curve over several values of the external rate. Simulations in **A** and **B** were calculated using the following parameters: $\nu = 8000$ Hz, $f^E = 0.23125$ mS/cm^2, $f^I = 0.4$ mS/cm^2.
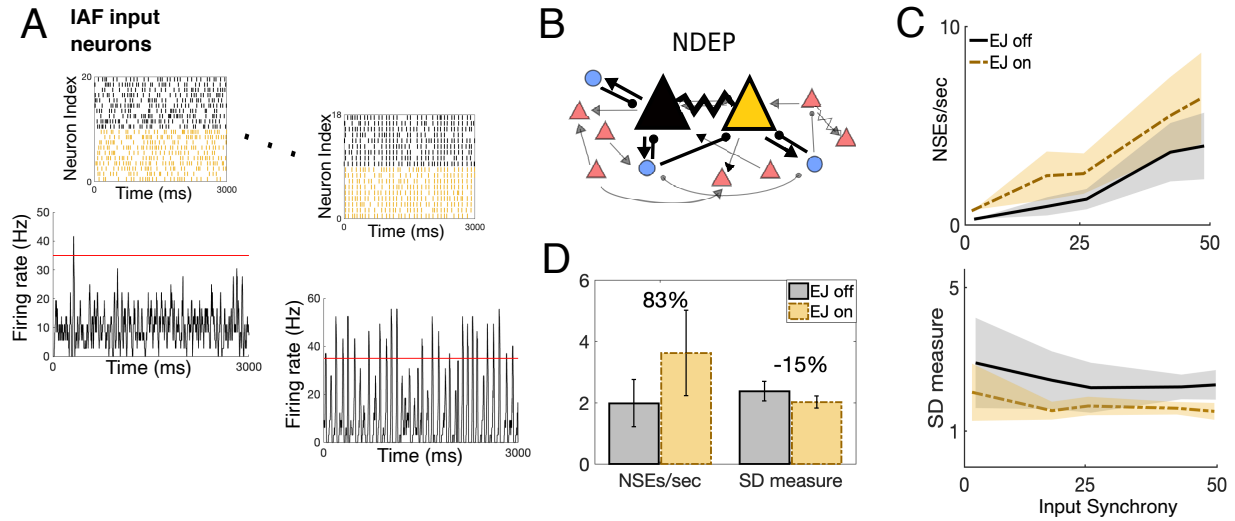

Figure 8: Schematic of the two-layer network. **A**: *Top:* Raster plots for an unsynchronized (left) and synchronized (right) IAF input network, with colors coordinating with the neuron in the NDEP to which it projects [see **B**]. *Bottom:* The instantaneous firing rate for each type of network is plotted below each raster with a threshold of 35 Hz plotted in red, used to determine the input synchrony measure. **B**: Schematic downstream HH network, with one NDEP shown enlarged and color coordinated with the spikes from the IAF network that are received by each neuron in the NDEP. The strength of the synaptic connections are illustrated by the weight of the line between each cell, with the arrow for excitation and ball for inhibition. **C**: *Top:* The number of NSEs per second for the EJ turned on (yellow, dash-dotted) and turned off (black, solid) and *Bottom:* the SD measure of all neurons in the network (except the NDEP) for the EJ turned on and off over a range of input synchrony values. The solid line indicates the average, while the shading indicates the standard deviation, over 30 realizations. **D**: The average difference in the SD measure and the NSEs/sec over all input synchrony values. The black bars indicate standard deviation.

chrony values, with the rate of increase for both the NDEP with the EJ turned on and off being similar.

Though the rate at which the number of NSEs increases with incoming synchrony is similar for the network with the EJ turned on and off, we observe that each NSE is more synchronized (exhibits a lower SD measure) when the NDEP has an EJ that is turned on, as compared to when it is turned off, as shown in the bottom panel of Fig. 8C. As demonstrated earlier (e.g., see Fig. 3), GJ-coupled networks tend to generate NSEs when a significant portion of the inhibitory neurons receive enough excitation to fire. Then, since the GJ has a large coupling probability and range, most inhibitory neurons are near threshold such that when a few neurons fire an action potential, the spikelet that occurs due to the GJ is enough to push some more to fire, and eventually the rest of the network will fire as well. When the NDEP has the EJ turned on, a subset of the inhibitory population receives excitatory spikes from two neurons that fire synchronously, as opposed to asynchronously when the EJ is turned off, and thus the cascade of firing in the inhibitory population occurs much more rapidly, yielding a more synchronized NSE.

The effect on these two synchrony measures (number of NSEs/sec and SD measure) of turning the EJ on and off is large, yielding an 83% increase in the average number of NSEs/sec over all input synchrony values, and a 15% decrease in the SD measure, from the network containing an NDEP with the EJ turned off to the network containing an NDEP with the EJ turned on; see Fig. 8D. These results combine to support the hypothesis that an NDEP with the EJ turned on requires a less synchronous sensory input to generate the same number of NSEs than an NDEP with EJ turned off, and that each NSE is itself more synchronized than when the EJ is turned off. Thus, we observe that the nonzero EJ creates an NDEP that reduces temporal jittering of spikes and enhances the associations between spike events.

As shown above, one PC pair with the EJ turned on may play an important role in regulating the network spiking events. However, in the cortex, several pairs of EJ-coupled PC pairs were detected. To this end, we introduce another NDEP into the downstream HH network and note that, in this situation, we consider two cases for the IAF input to the two NDEPs. One is the case in which the two NDEPs receive input from the same network of upstream neurons (same IAF input). In this case, the spikes received by each NDEP will be similarly timed since they will have originated from one network. Another case is one in which the NDEPs receive input from patches of the upstream IAF network that are operating as separate subnet-

works (different IAF input). In this case, the spikes received by each NDEP will have similar statistics, but will originate from different realizations of the IAF network, and thus may have different spike timings. We analyze the downstream network behavior in both cases.

First, we note that each NDEP independently behaves similarly to the one-NDEP case, generating more NSEs that are each more tightly synchronized than those generated by an NDEP with EJ turned off; see Fig. 9A and compare blue and red bars to grey bar. These effects are on the same order as those seen in the one-NDEP case, with percent changes from a network with EJ turned off to a network with EJ turned on averaging about 80% for the number of NSEs per second and -15% for the SD measure; see Fig. 9B. We note that, however, the two cases of IAF inputs generate different results for the number of NSEs, both of which are smaller than the case of simply doubling the number of NSEs that is measured for the one-NDEP case (compare blue and red bars to green bar in Fig. 9A). This suggests that there may be interactions between the two NDEPs that result in inhibition of the firing of the network in some cases (since the number of NSEs is less than double the number from the one-NDEP case), see Ref. [8] for more details on this interaction.

We analyze this interaction by measuring how the spike pattern of the network differs between the one-NDEP regime and the two input cases for the two-NDEP regime. To do this, we calculate the average firing rate of the excitatory neurons over the course of the simulation and find times at which this average firing rate crosses a threshold of 1 Hz; see Fig. 9C. These crossings might represent times at which the excitatory population is sufficiently synchronized to send information to further downstream areas. We choose those simulations that have similar firing rates (average over four regimes is 2.87 Hz with a standard deviation of 0.21 Hz) to ensure that the variability in the spiking pattern is not due to changes in the firing rate. To understand how the coding of information might change for each coupling regime, we calculate the time difference between excitatory neurons' firing events and plot a histogram of the time differences; see Fig. 9D, paying particular attention to the CV value of each histogram. Notice that the CV value for the network containing two NDEPs receiving the same IAF input (0.77) is higher than for the networks with no EJ (0.49) and one NDEP (0.53), reflecting higher firing variability in the network containing two NDEPs. The nontrivial interaction between two NDEPs, especially in the case when input to each NDEP originates in different IAF input net-

works, results in a network that has a highly variable firing pattern, allowing the network to have a larger coding capacity.

Discussion

In this work, we develop a point neuron model that reproduces experimentally-observed behavior measured from pairs of GJ-coupled FS cells and EJ-coupled PCs. Using this model, and organizing the neurons into a network, we show that, in the mean-dominated regime, synchrony and oscillations naturally arise with the addition of ubiquitous GJ-coupling among the FS cells. This property of dendro-dendritic gap junctions has been observed experimentally, as well as demonstrated mathematically [3, 7, 26, 27]. With the addition of pair-wise EJs between PCs, however, the network appears to exhibit little to no change in its global dynamics. We show that the measured effects on synchrony and oscillations are small, less than a 7% change on average, and on the order of the network fluctuations. Then, we study the fluctuation-dominated regime in which the network firing pattern is much more irregular. The addition of GJ-coupling in this regime elicits little network synchrony and no oscillations. In this regime, we investigate how the regularity of the firing pattern changes with the addition of EJs to networks that do and do not contain GJ coupling. Using the inter-spike interval (IS) and the coefficient of variation (CV), we show that the addition of GJ coupling decreases the average time between spikes (increases the firing rate) and increases the regularity of the firing (decreases the CV). With the addition of EJ coupling between pairs of PCs, we do not observe any significant change in the firing rate or the firing pattern of the network; again, any observed changes are on the order of network fluctuations.

With the goal of understanding what role pair-wise EJs might play in influencing network dynamics, we next investigate how the firing pattern of the pairs of PCs themselves are affected by the addition of an EJ. In this case, we show a very significant increase in the synchrony between the spiking of these pairs of neurons with the addition of EJ coupling. Note that the spiking dynamics of the EJ-coupled pair of cells differs from that of a synaptically-coupled pair of PCs in that the synchrony is much stronger and the firing rate is much higher (due to the fast transmission of the electrical junction) leading to fast-frequency oscillations. We show that this increased synchrony may be responsible for recruiting more FS cells into each synchronous event, though this change is small, less
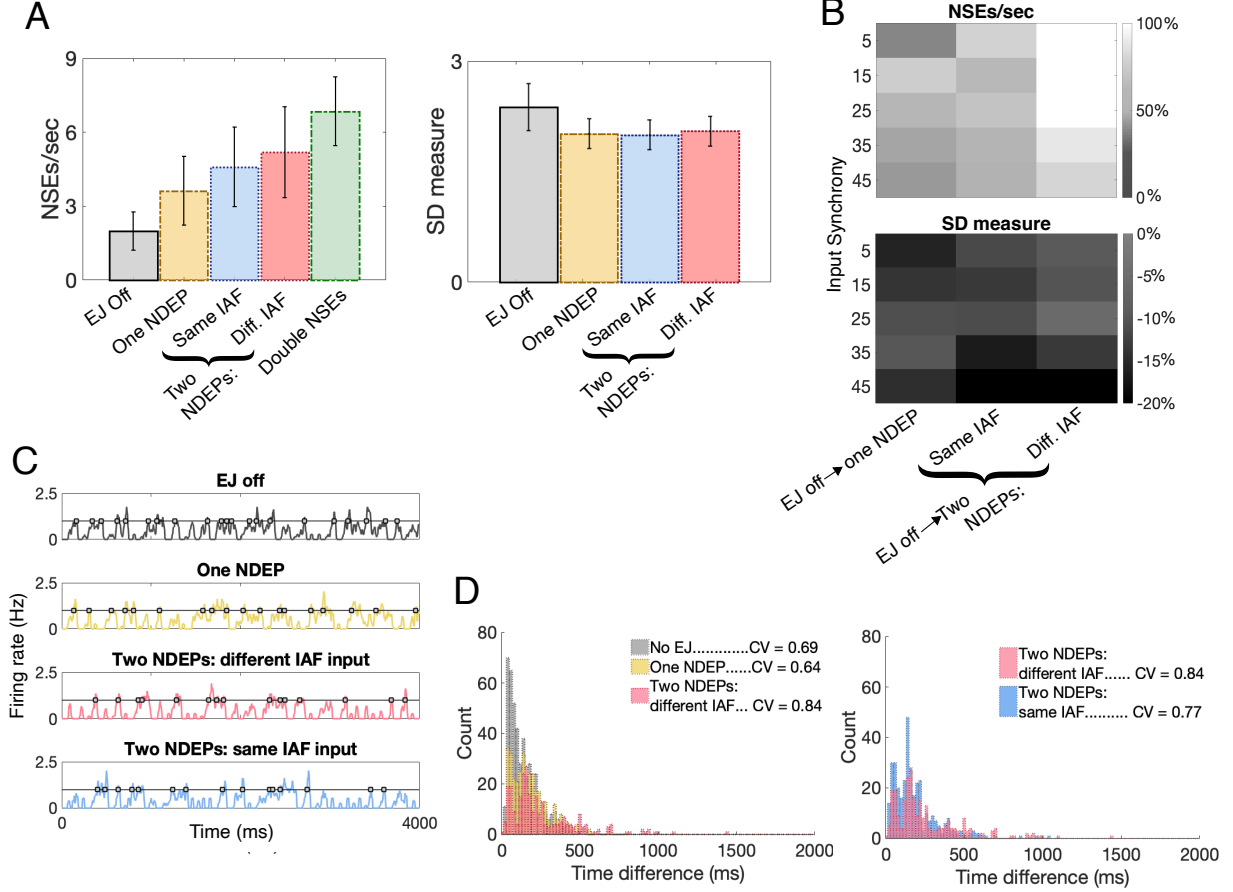
Figure 9: Comparison of one- and two-NDEP networks for each network regime: EJ turned off (no EJ), EJ turned on (one NDEP), two NDEPs with input from the same IAF upstream network, and two NDEPs receiving input from neurons in different IAF networks. **A** *Left:* The number of NSEs per second averaged over all input synchrony values, with an additional comparison to a hypothetical network in which the number of NSEs is doubled from the one-NDEP case. *Right:* The SD measure for each regime averaged over all input synchrony values. **B**: The percent change from a network with the EJ turned off to the EJ turned on, for all network regimes. **C**: The instantaneous firing rate of the excitatory neurons in each coupling regime. **D**: *Left:* Histogram of time differences between excitatory neurons' spiking events [defined in **C**] comparing one NDEP (yellow), EJ turned off (grey), and two NDEPs receiving different IAF input (red). *Right:* Histogram of time differences between excitatory neurons' spiking events [defined in **C**] comparing two NDEPs receiving different IAF input (red) and the same IAF input (blue).

than 5%. Since we have shown that sparse and random synaptic connectivity among the neurons does not allow for significant changes in the network dynamics due to the inclusion of EJ coupling, we form a new network in which the synaptic connections from the EJ-coupled PCs to the inhibitory neurons (and back) are enhanced. In this new network, we show that the addition of EJ coupling increases the number of synchronous events in the network and, additionally, each event is yet more synchronized than those that are generated in a network without EJ coupling. Importantly, the presence of two NDEPs in the network does not simply result in twice the number of synchronous events, but instead allows for interactions between the events, resulting in a network with a highly variable firing pattern. This potential functional role of EJ-coupling in information processing relies upon the tight, precise synchrony that occurs between the EJ-coupled cells. In addition, synchronized network dynamics may arise more readily from networks which contain EJ-coupling compared to those that do not (see Ref. [8] for an investigation of EJ-coupled PCs organizing network dynamics).

Electrotonic junctions have been observed in many

brain regions, their properties have been measured, and their functional roles have been proposed. In the hippocampus, for example, EJ coupling has been shown to be involved in fast-frequency oscillations when networks of PCs are extensively coupled axo-axonally [28]. Additionally, EJ coupling among PCs in the neocortex has been proposed to play a role in generating spatiotemporal patterns of fast-frequency oscillations when the PCs are interconnected with EJs [14, 29]. During cortical development, experimentalists have also found EJs among PCs [19]. In the mouse visual cortex, for example, experiments have shown that EJs couple PCs that originate from the same progenitor cell [32]. During the embryonic stage, while cells are migrating to the cortical plate, EJs between PCs have been shown to be important for successful migration to the correct location [9]. Once the mouse is born, however, the role of the junction remains unclear. Additionally, during the first postnatal week, the coupling strength of this junction decreases such that no couplings are found by the second post-natal week [32].

In the adult cortex, however, measurements of EJs between PCs have been scant, leading to a controversy over their existence and possible functional role. The most extensive experiment to date, by Wang et al. [31], measured rare, pair-wise couplings of cells whose soma are either touching or overlapping, which may explain the experimental difficulty in reproducing the study. In addition, this study found putative contacts between the dendrites of some EJ-coupled cells and the axons of other EJ-coupled cells. In this work, we use a point-neuron model to show that pair-wise coupling of PCs with experimentally-determined junctional strength results in synchrony and fast-frequency oscillations, similarly to networks of EJ-coupled PCs in the hippocampus, but of just those two coupled cells. Using typical network coupling probabilities and strengths, we do not observe a significant change in the network behavior due to the addition of EJ-coupled pairs of PCs, suggesting no functional role for these pairs and no further support for their existence. It should be noted that the location of the EJ along either the dendrites or the axons of coupled PCs could change the behavior, and thus the function and network effect, of EJ-coupled PCs. It is known that the dendrite has a filtering effect for the voltage response due to its cable properties. Namely, the magnitude of the voltage can be very different between the soma and the dendritic site, thus leading to different electrical currents received by the postsynaptic neuron. In addition, it has been recently found that nonlinear interactions exist among synaptic currents in both passive and active dendrites [35]. It is expected that similar nonlinear interactions could also exist between the electrical currents and synaptic currents. Nevertheless, it would be interesting to investigate the location effect (at the soma or the dendritic site) of electrical coupling on neuronal network dynamics and further analysis of a more detailed, spatial neuron model would be required.

Another possible conclusion one can draw from these results is that the EJs measured by Wang et al. [31] in the adult cortex are simply a relic of those present during the first post-natal week of development. The coupling strength measured by Wang et al. [31], however, is much larger than the one reported for EJs during development (CC of 50% in adult compared to 7% in development [32]), suggesting that the junctions measured in the adult cortex may be different from those measured during development. Assuming instead that these junctions are not simply left over from development, and exist in the adult cortex for some purpose, a third conclusion one can draw is that pairs of EJ-coupled PCs may have a functional role in reducing noise in incoming stimuli, producing synchronized network events, and increasing network coding capacity. Although increased synaptic connectivity between EJ-coupled cells and the FS cells has not explicitly been measured, it could be plausible that this type of synaptic coupling can come about from Hebbian plasticity due to the correlated firing activity between EJ-coupled PCs and GJ-coupled FS cells, leading to an enhanced synaptic connection. In addition, these rare, strong synapses may not show up in the average sparse connectivity reported by experimentalists.

Acknowledgments

Appendix

In this Appendix, we describe the process by which parameter values for the FS cells and PCs in the cortical network are chosen. Included in each section is evidence that those parameter choices lead to neuron behavior similar to experimentally-measured behavior for electrically-coupled neurons of each type.

Parameter Choices

We choose parameter values for the HH model of the downstream cortical network to qualitatively match experimentally-observed voltage traces of FS cells and PCs. In particular, we fix the following parameters: the capacitance C, resting voltage v_R, sodium reversal potential v_{Na}, and potassium reversal potential v_K at the values shown in Table 1 in the main text, and vary all other neuron parameters within the ranges described in Table 4. Then, we choose values for these parameters within those ranges based on qualitatively matching voltage traces to experiments. Note that, due to sensitivity in measuring equipment and procedural differences in collecting data across labs, we do not attempt a more quantitative match. Rather, we demonstrate that our model neurons behave similarly to experiments in response to different external input and reproduce phenomena unique to GJ-coupled FS cells and EJ-coupled PCs in the adult cortex.

Table 4: Parameters ranges extracted from experiments [10, 12, 22, 31]. The ranges for the junctional conductance, g_C, were determined from reported values of the conductance in units of nS and converted to mS/cm^2 using a diameter of 56.9 μm for FS cells and 96 μm for PCs, as estimated in Ref. [22].

Parameter Range	FS cells	PCs
g_L (mS/cm^2)	$0.02 - 0.2$	$0.01 - 0.1$
$\bar{g}_{Na}$ (mS/cm^2)	$30 - 60$	$30 - 60$
$\bar{g}_K$ (mS/cm^2)	$3.9 - 7.0$	$2.0 - 6.0$
V_T (mV)	-60 − -56	-65 − -50
g_C (mS/cm^2)	$0.0026 - 0.028$	$0.03 - 0.09$

Matching experimental results: *FS Cells*

For GJ-coupled FS cortical cells, we use the experimental results from Refs. [10, 11] to determine the leakage conductance, g_L, which controls the sub-threshold voltage decay back to rest after a depolarization or hyperpolarization; the maximal sodium and potassium conductances, $\bar{g}_{Na}$ and $\bar{g}_K$, respectively, which control the rise and fall of the action potential, respectively; and the GJ conductance, g_C, which controls the amount of information that is transmitted through the junction.

We begin by investigating how the leakage conductance affects the sub-threshold voltage decay of an FS neuron after a sub-threshold depolarization and hyperpolarization. Note that since the potassium and sodium channels are essentially closed unless the neuron is firing an action potential, we set $\bar{g}_{Na}$ and $\bar{g}_K$ to zero to investigate sub-threshold effects. The experiments by Galarreta and Hestrin [10, 11] show that a GJ-coupled FS cell exhibits a decay time of about 50 ms in response to a constant current input for 100 ms that raises the voltage about ± 10 mV from rest for depolarization and hyperpolarization protocols. To replicate this experiment in our model, we inject a constant current to our FS cells of strength $I_{\text{const}} = \pm$ 0.5 mA/cm^2. Figure 10A shows the voltage traces of the FS cell in response to hyperpolarization and depolarization for several values of g_L, together with a table of decay times for each value.

We fix the leakage conductance at $g_L = 0.1$ mS/cm^2 and, while still considering the neuron's sub-threshold behavior, begin to narrow down the choice for the GJ conductance, g_C. Experiments show that the coupling coefficient (CC), or the ratio of the change in post-junctional voltage to the change in pre-junctional voltage, for GJ-coupled FS cells is about 10% [10]. Figure 10B shows the pre-junctional (solid curves) and post-junctional (dashed curves) voltage changes for several values of the GJ conductance, with the resulting coupling coefficient shown in the corresponding table. Note that several values of the GJ conductance ($g_C = 0.01 - 0.015$) yield CC values near 10%. Therefore, we use the spiking behavior of the cells to further narrow down this parameter choice.

To match the spiking behavior of FS cells, we use voltage traces measured in Ref. [31]. In the model, three parameters control the action potential shape: the spiking threshold, v_T; the maximal sodium conductance, $\bar{g}_{Na}$; and the maximal potassium conductance, $\bar{g}_K$. We begin with the spiking threshold, v_T, keeping the sodium and potassium maximal conduc-
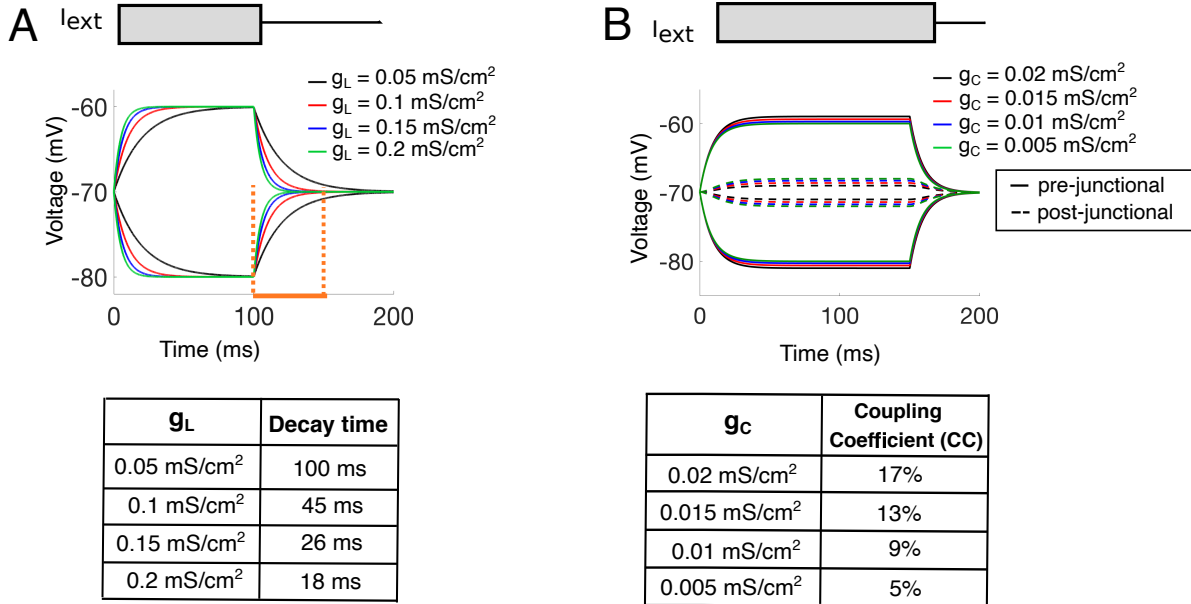
Figure 10: Sub-threshold voltage traces for FS cells. **A**: Voltage traces, together with a table of the decay time to rest, for various values of g_L. The decay time is calculated as the time it takes for the voltage to decay from its value at the time the stimulus is turned off (100 ms) to within 0.5 mV of the resting potential. **B**: Voltage traces, together with a table of values of the coupling coefficient (ratio of the voltage change in the post-junctional cell to the voltage change in the pre-junctional cell), for various values of g_C. The external drive for these figures is $I = \pm 0.5$ mA

tances near their respective averages of 45 mS/cm^2 and 5 mS/cm^2.

In the experiments, the sub-threshold voltage begins a sharp increase around -45 mV. We mark this location in our model simulation and look for the value of v_T that gives a sub-threshold increase until around -45 mV and then begins its ascent to the spike; see Fig. 11A. Experimental traces show that the spike decreases to about -62 mV and increases to a height of about 20 mV, giving indicators for our choices of $\bar{g}_K$ and $\bar{g}_{Na}$, respectively. We mark those locations in our model simulations, and vary the values for the sodium and potassium conductances; see Fig. 11B and C.

To narrow down the choice of the GJ conductance, we consider the spikelet amplitude, or the height of the post-junctional voltage increase in response to a pre-junctional action potential; ; see Fig. 11D. Note that the experimentally-measured spikelet amplitude is 1.5 ± 0.2 mV, as reported in Ref. [31]. The final parameter choices are shown in Table 1 in the main text.

Reproducing experimental phenomena: FS cells

In this section, we show that our model, with the chosen parameters, captures experimental phenomena exhibited by GJ-coupled cortical FS cells. We note that these parameter choices are not unique and the results do not vary with reasonable changes in these parameters.

The phenomena that we choose to replicate are from the experiments by Galarreta and Hestrin [10] in which they demonstrate the behavior of two GJ-coupled FS cells by injecting current into one cell and observing the effect in the coupled cell. First, Galarreta and Hestrin show that GJs act as low-pass filters, preferentially transmitting low-frequency signals, by injecting a sine-wave current into the pre-junctional cell and showing that the CC of the post-junctional cell decreases as the frequency of the sinusoidal input increases. They also demonstrate that the spikelet in the post-junctional cell exhibits a phase lag that increases with increasing input frequency. In response to a sinusoidal input, our model captures this phenomenon as well; see Fig. 12A. In response to increasing frequency, our model behaves similarly to experiments, with an increase in phase lag, and de-
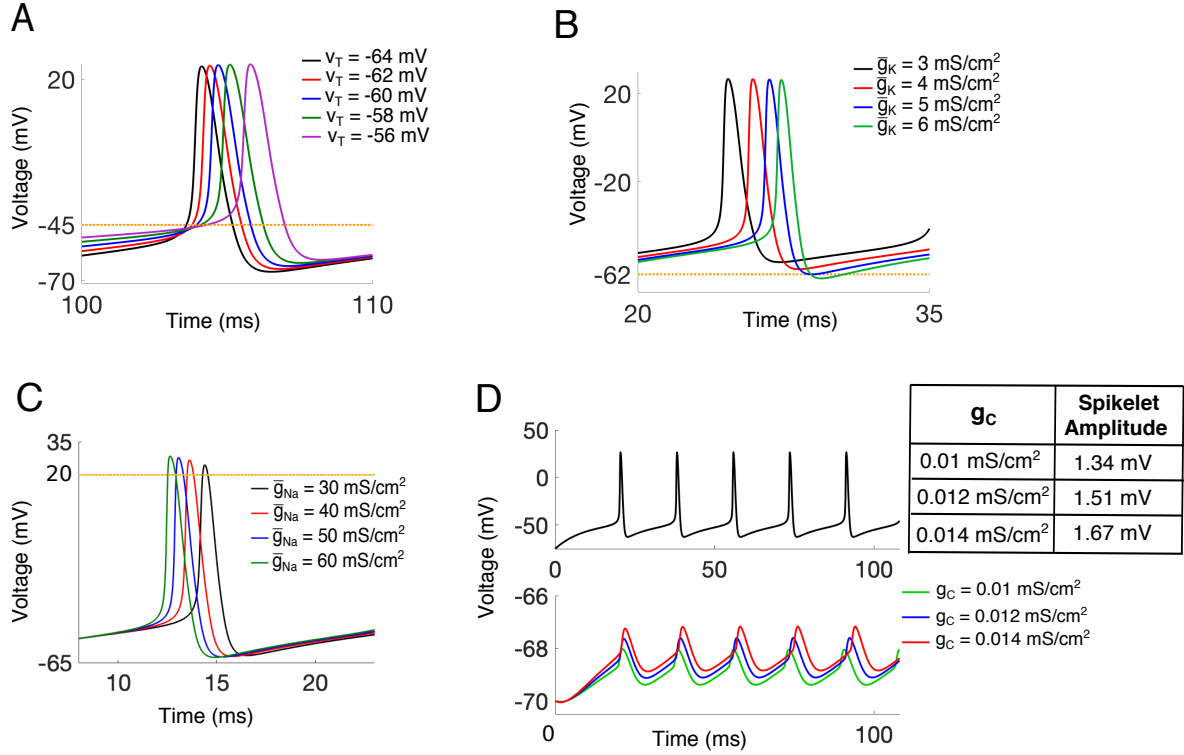
Figure 11: Action-potential model replications for FS cells. **A**: Model action potential shape for various values of the spiking threshold, v_T. The orange dotted line denotes the experimentally-estimated threshold. **B-C**: Action potential shapes as a result of various values of the maximal potassium conductance, $\bar{g}_K$, and the maximal sodium conductance, $\bar{g}_{Na}$, respectively. The orange dotted line in **B** and **C** denotes the experimentally-estimated value for the maximal decay of the action potential and maximal peak of the action potential, respectively. **D**: Model voltage trace for pre-junctional cell action potentials in response to constant current input and the resulting spikelets in the post-junctional cell, together with a table of the spikelet amplitude, for various values of g_C. The constant current input used here is $I = 3.0 \text{ mS/cm}^2$.

crease in coupling coefficient, as frequency increases; see Fig. 12B. Note that the frequency at which these curves cross occurs near the same location as in the experiments.

Galarreta and Hestrin [10, 11] also demonstrated that a high-frequency train of action potentials in the pre-junctional cell is transmitted as a short summation of spikelets in the post-junctional cell when the post-junctional cell is hyperpolarized to a value below the resting potential. Our model qualitatively reproduces this phenomenon as well; see Fig. 12C. Finally, Galarreta and Hestrin demonstrate that there is a delay between the peak of the action potential in the pre-junctional cell and the peak of the spikelet in the post-junctional cell, which our model reproduces in Fig. 12D.

Matching experimental results: *Pyramidal Cells (PCs)*

We utilize similar techniques as in the previous section for a pair of PCs coupled by an EJ with the aim of replicating experimental data described by Wang et al. [31]. We begin again with the sub-threshold dynamics by setting both $\bar{g}_{Na}$ and $\bar{g}_K$ to 0 and considering different values for the leakage conductance, g_L. Experiments show that PCs have a decay time for sub-threshold voltage of about 200 ms in response to a hyperpolarization and depolarization of about ± 20 mV. We perform a similar task in our model neuron; see Fig. 13A.

Experiments show that EJ-coupled PCs have a CC of about 60%. Therefore, we vary the EJ conductance, g_C, and show that there are several values of the conductance for which the coupling coefficient is near 60%; see Fig. 13B. Wang et al. [31] also measured very little dependence of the EJ conductance on the membrane potential of either cell, which can be demonstrated by calculating the amplitude of the pre-junctional and post-junctional voltage difference from rest at several different values of the membrane potential. Our model reconstructs this independence of the junctional conductance on membrane potential as well, and we calculate the slope of the line; see Fig. 13C (0.8 as measured experimentally). As in the case of FS cells, we use the spiking behavior of PCs to narrow down the choice for the EJ conductance.

Next, we consider the spiking dynamics of a pair of EJ-coupled PCs. First, observe that action potentials have a different shape in response to a constant current input as compared to a 20-Hz spike train, as shown in Ref. [31]. Therefore, we consider both types of input and use characteristics of the action potentials generated in each case to determine val-

ues for v_T, $\bar{g}_{Na}$, and $\bar{g}_K$. Note that to simulate a spike train, we input constant-current step pulses into the pre-junctional cell at a particular frequency such that the pre-junctional cell fires one spike per current pulse. We do not include any stochasticity in these matching experiments.

The spiking threshold is chosen by considering the voltage at which the action potential begins its ascent in response to a constant-current input, as shown by the orange dotted line in Fig. 14A (top), and a high voltage of the tail of the action potential in response to a 20-Hz spiking input, as shown in Fig. 14B (bottom). The maximal sodium and potassium conductances, $\bar{g}_{Na}$ and $\bar{g}_K$, respectively, are chosen by matching spiking dynamics in the 20-Hz spike-train case with the aim of obtaining a very fast rise and a slow decay, as was observed experimentally by Wang et al. [31].

We choose the conductance of the EJ by matching the spikelet amplitude of 14 mV as measured experimentally. Notice that an EJ conductance value of 0.08 mS/cm^2 gives a spikelet amplitude of 15 mV, and is within reason with respect to the sub-threshold dynamics (recall Figs. 13B and C). The final parameter set is shown in Table 1 in the main text.
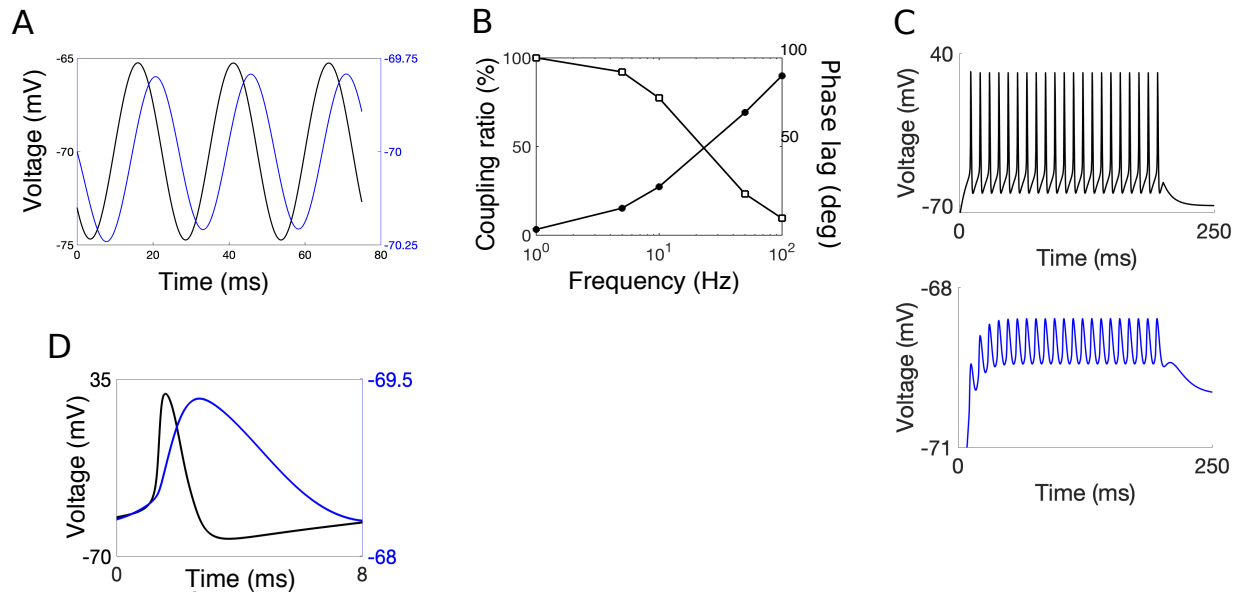
Figure 12: Reproducing experimentally-observed phenomena for FS cells. **A**: Voltage responses in pre- (black) and post- (blue) junctional cells due to a sinusoidal input to the pre-junctional cell. The left axis describes the pre-junctional voltage, while the right axis shows the post-junctional voltage. **B**: The frequency dependency of the coupling coefficient (open squares) and phase lag (closed circles) for GJ-coupled cells. **C**: Action potentials in the pre-junctional cell (black) result in a short summation of spikelets in the post-junctional cell (blue) if the membrane potential of the post-junctional cell is hyperpolarized to a value below the resting potential (-72 mV in the model). **D**: Superimposed action potential from the pre-junctional cell (black) with the spikelet of the post-junctional cell (blue). Axes labels are color coded for which curve they represent.

Reproducing experimental phenomena: *PCs*

We show that our model of two EJ-coupled PCs captures experimental phenomena observed by Wang et al. [31], including responses to high frequency stimuli and spikelet summation. Due to the high junctional conductance, Wang et al. [31] recorded that spikelets in the post-junctional cell sum to threshold in response to a high-frequency (70 Hz) stimulation of action potentials in the pre-junctional cell. Our model PCs mimic this behavior in response to a 70-Hz input stimulus; see Fig. 15A. To quantify this summation, Wang et al. [31] calculated a second summation rate, the ratio of the difference in height between the second and the first spikelet to the height of the first spikelet. Wang et al. [31] showed that, across all measured EJ-coupled PC pairs, this second-summation rate increases with an increase in stimulation frequency to the pre-junctional cell. Our model also shows this increase in summation rate; see Fig. 15B. In addition, experiments indicate that the amplitude of the post-junctional spikelet has very little dependence on the membrane potential of the post-junctional cell. Our model replicates this small dependence of the spikelet amplitude on the membrane potential of the post-junctional cell, with a slightly higher spikelet amplitude than experimentally observed in all cases; see Fig. 15C.

Action potentials in the pre-junctional cell result in spikelets in the post-junctional cell with an amplitude of about 14 mV, recall Fig. 14C. However, Wang et al. [31] measured that in response to a 20-Hz spike train in the pre-junctional cell, the post-junctional cell will spike about 50% of the time that the pre-junctional cells spikes. We show that our model captures this phenomenon; see Fig. 15D for a few simulated milliseconds. If we run the simulation for 10 seconds and calculate the ratio of number times an action potential in the post-junctional cell occurs to the number of times an action potential in the pre-junctional cell occurs, the result is 54%. Though Wang et al. did not measure the coupling coefficient as a function of stimulation frequency, we use our model to show that EJs behave similarly to GJs in this respect; see Fig. 15E.
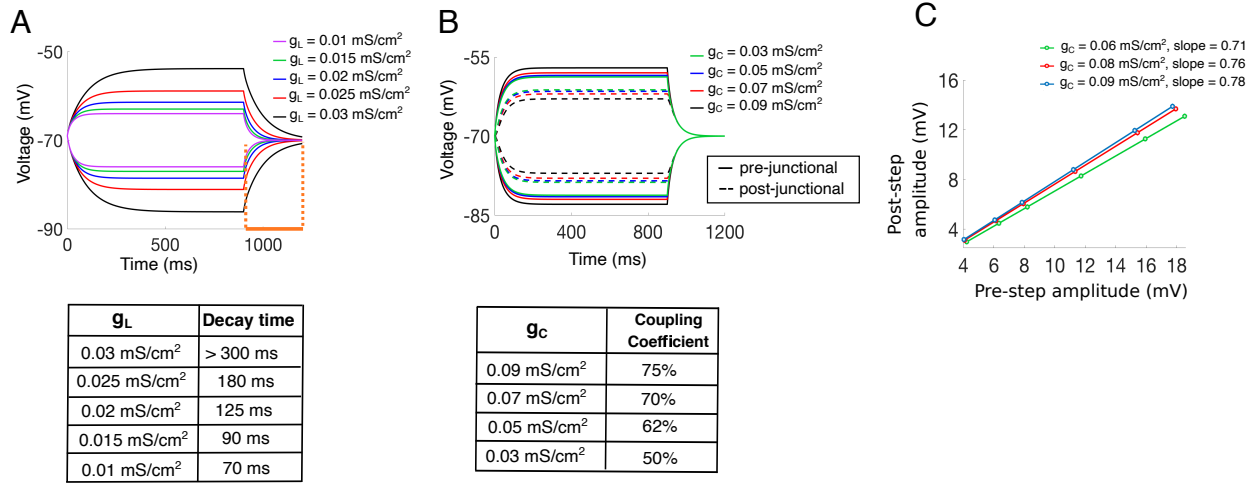
21

Figure 13: Sub-threshold voltage-trace model replications for PCs. **A**: Voltage traces from model PCs, together with a table of decay times, for various values of g_L. **B**: Voltage traces from model PCs, together with a table of values for the coupling coefficient (ratio of the change in voltage of the post-junctional cell to the voltage change in the pre-junctional cell), for various values of g_C. **C**: The relationship between the amplitude of the post-junctional cell and the pre-junctional voltage amplitude for three values of the EJ conductance.
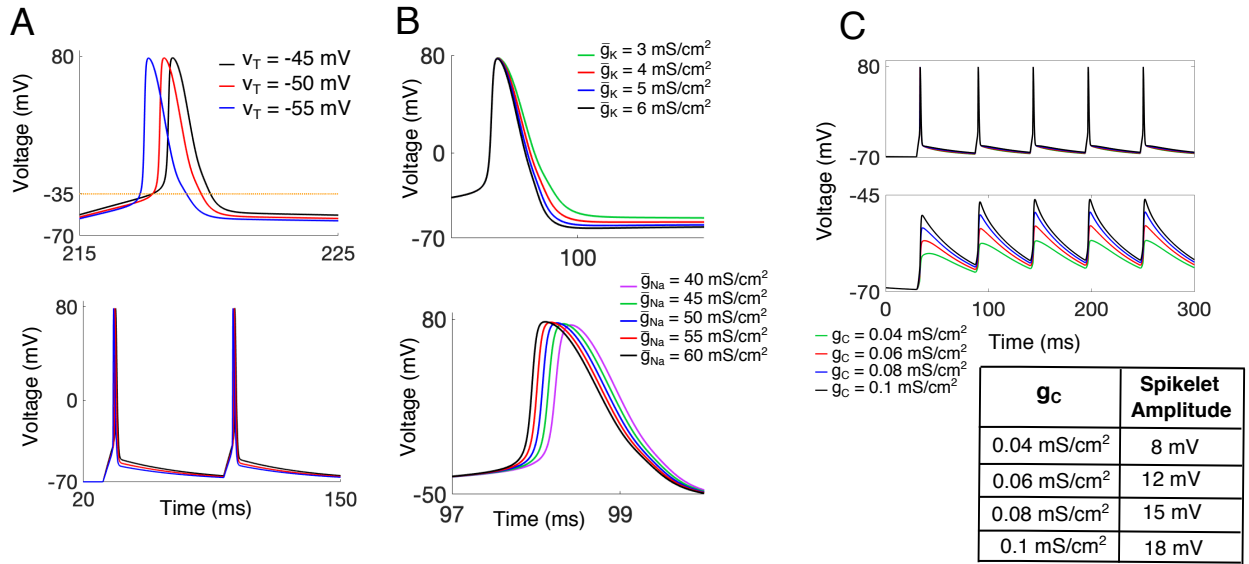

Figure 14: Action-potential model replications for PCs. **A**: Model action potential shape for various values of the spiking threshold, v_T, for a constant current input (top) and a 20-Hz stimulus (bottom). The orange dotted line denotes the experimentally-estimated value for the voltage at which the action potential begins. **B**: Action-potential shapes as a result of various values of the maximal potassium conductance, $\bar{g}_K$, (top) and the maximal sodium conductance, $\bar{g}_{Na}$, (bottom). **C**: Model voltage trace of pre-junctional action potentials in response to 20 Hz input and corresponding spikelets in the post-junctional cell, together with a table of spikelet amplitudes, resulting from various values of g_C.
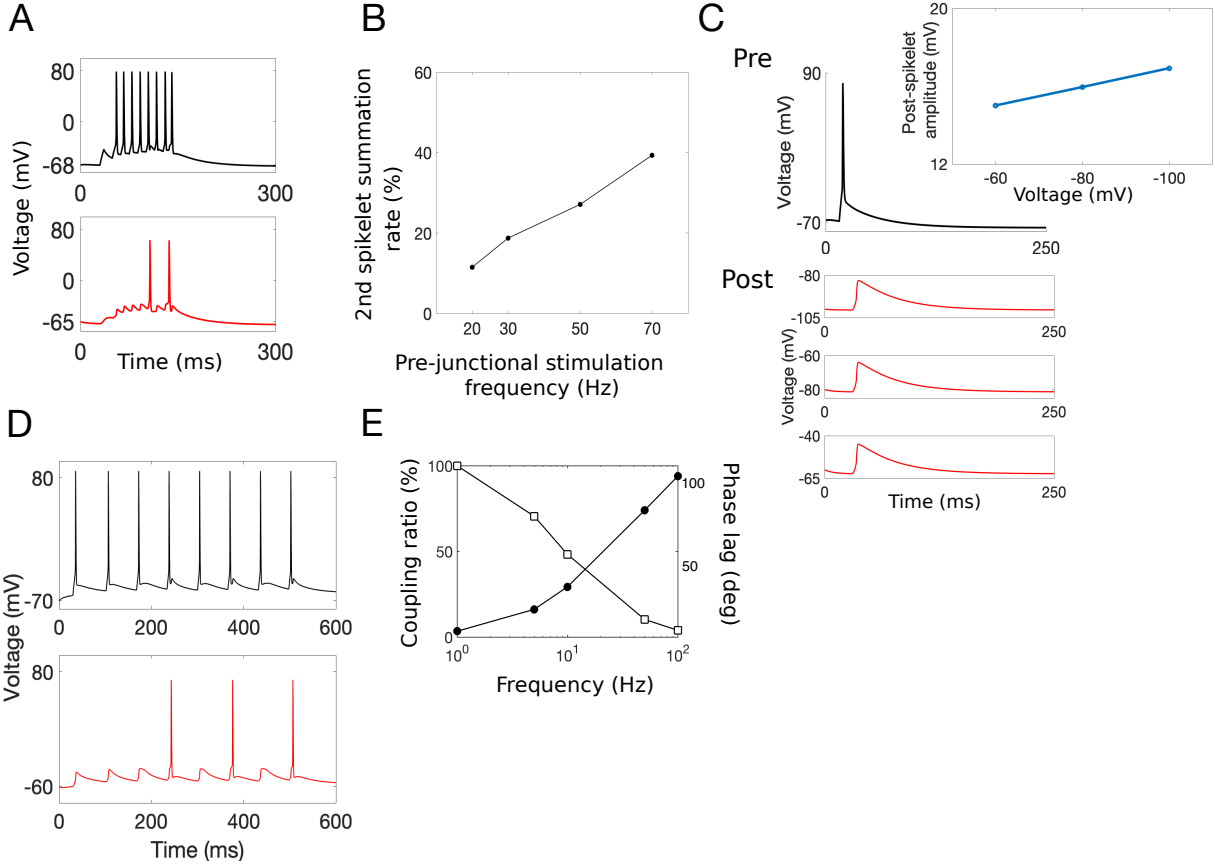
22

Figure 15: Replicating experimental phenomena for PCs. **A**: Model voltage traces in response to a 70 Hz signal for pre-(black) and post- (red) junctional PCs. **B**: The second summation spikelet rate – a measure for the change in height from the first spikelet to the second – as a function of the stimulation frequency to the pre-junctional neuron for the model pair of PCs. **C**: The amplitude of the post-junctional spikelet for different voltages of the post-junctional cell. **D**: Action potentials in the pre-junctional cell (black, top) in response to a 20-Hz input and the response in the post-junctional cell (red, bottom) when it is depolarized to -60 mV. **E**: The frequency dependency of the coupling coefficient or ratio (open squares) and phase lag (closed circles) for EJ-coupled PCs. Parameters used to generate these figures are those listed in Table 1, together with the following values: for **A**, the constant external input is $I = 6$ mA and input frequency is 70 Hz; for **D**, the constant external drive is $I = 8$ mA and input frequency is 20 Hz; and for **E**, the constant external input is $I = 10$ mA.

References

[1] Yael Amitai, Jay R Gibson, Michael Beierlein, Saundra L Patrick, Alice M Ho, Barry W Connors, and David Golomb. The spatial dimensions of electrically coupled networks of interneurons in the neocortex. *J. Neurosci.*, 22(10):4142–4152, May 2002.

[2] C Beaulieu. Numerical data on neocortical neurons in adult rat, with special reference to the gaba population. *Brain Res*, 609(1-2):284–292, Apr 1993.

[3] M Beierlein, J R Gibson, and B W Connors. A network of electrically coupled interneurons drives synchronized inhibition in neocortex. *Nat Neurosci*, 3(9):904–910, Sep 2000.

[4] Michael V L Bennett and R Suzanne Zukin. Electrical coupling and neuronal synchronization in the mammalian brain. *Neuron*, 41(4):495–511, Feb 2004.

[5] David Cai, Aaditya V. Rangan, and David W. McLaughlin. Architectural and synaptic mechanisms underlying coherent spontaneous activity in v1. *Proceedings of the National Academy of Sciences*, 102(16):5868–5873, 2005.

[6] C C Chow and N Kopell. Dynamics of spiking neurons with electrical coupling. *Neural Comput.*, 12(7):1643–1678, Jul 2000.

[7] Barry W Connors. Synchrony and so much more: Diverse roles for electrical synapses in neural circuits. *Dev Neurobiol*, 77(5):610–624, May 2017.

[8] Jennifer Crodelle, Douglas Zhou, Gregor Kovačič, and David Cai. A role for electrotonic coupling between cortical pyramidal cells. *Frontiers in Computational Neuroscience*, 13:33, 2019.

[9] Laura A B Elias, Doris D Wang, and Arnold R Kriegstein. Gap junction adhesion is necessary for radial migration in the neocortex. *Nature*, 448(7156):901–907, Aug 2007.

[10] M Galarreta and S Hestrin. A network of fast-spiking cells in the neocortex connected by electrical synapses. *Nature*, 402(6757):72–75, Nov 1999.

[11] M Galarreta and S Hestrin. Electrical synapses between gaba-releasing interneurons. *Nat. Rev. Neurosci.*, 2(6):425–433, Jun 2001.

[12] J R Gibson, M Beierlein, and B W Connors. Two networks of electrically coupled inhibitory neurons in neocortex. *Nature*, 402(6757):75–79, Nov 1999.

[13] D Johnston and T H Brown. Interpretation of voltage-clamp measurements in hippocampal neurons. *J. Neurophysiol.*, 50(2):464–486, Aug 1983.

[14] T J Lewis and J Rinzel. Self-organized synchronous oscillations in a network of excitable cells coupled by gap junctions. *Network*, 11(4):299–320, Nov 2000.

[15] Timothy J Lewis and John Rinzel. Dynamics of spiking neurons connected by both inhibitory and electrical coupling. *J. Comput. Neurosci.*, 14(3):283–309, May-Jun 2003.

[16] D McLaughlin, R Shapley, M Shelley, and D J Wielaard. A neuronal network model of macaque primary visual cortex (v1): orientation selectivity and dynamics in the input layer $4c\alpha$. *Proc. Natl. Acad. Sci. U.S.A.*, 97(14):8087–8092, Jul 2000.

[17] Audrey Mercer, A Peter Bannister, and Alex M Thomson. Electrical coupling between pyramidal cells in adult cortical regions. *Brain Cell Biol.*, 35(1):13–27, Feb 2006.

[18] James I Nagy, Alberto E Pereda, and John E Rash. Electrical synapses in mammalian cns: Past eras, present focus and future directions. *Biochim Biophys Acta Biomembr*, 1860(1):102–123, Jan 2018.

[19] Dragos Niculescu and Christian Lohmann. Gap junctions in developing thalamic and neocortical neuronal networks. *Cerebral cortex (New York, N.Y. : 1991)*, 24, 07 2013.

[20] Srdjan Ostojic, Nicolas Brunel, and Vincent Hakim. Synchronization properties of networks of electrically coupled neurons in the presence of noise and heterogeneities. *J. Comput. Neurosci.*, 26(3):369–392, Jun 2009.

[21] Benjamin Pfeuty, German Mato, David Golomb, and David Hansel. Electrical synapses and synchrony: the role of intrinsic currents. *J. Neurosci.*, 23(15):6280–6294, Jul 2003.

[22] Martin Pospischil, Maria Toledo-Rodriguez, Cyril Monier, Zuzanna Piwkowska, Thierry Bal, Yves Fregnac, Henry Markram, and Alain Destexhe. Minimal Hodgkin-Huxley type models for

different classes of cortical and thalamic neurons. *Biol. Cybern.*, 99(4-5):427–441, Nov 2008.

[23] M J Shelley and L Tao. Efficient and accurate time-stepping schemes for integrate-and-fire neuronal networks. *J. Comput. Neurosci.*, 11(2):111–119, Sep-Oct 2001.

[24] M Srinivas, R Rozental, T Kojima, R Dermietzel, M Mehler, D F Condorelli, J A Kessler, and D C Spray. Functional properties of channels formed by the neuronal gap junction protein connexin36. *J. Neurosci.*, 19(22):9848–9855, Nov 1999.

[25] Yi Sun, Douglas Zhou, Aaditya V Rangan, and David Cai. Pseudo-lyapunov exponents and predictability of hodgkin-huxley neuronal network dynamics. *J. Comput. Neurosci.*, 28(2):247–266, Apr 2010.

[26] G Tamas, E H Buhl, A Lorincz, and P Somogyi. Proximally targeted gabaergic synapses and gap junctions synchronize cortical interneurons. *Nat. Neurosci.*, 3(4):366–371, Apr 2000.

[27] R D Traub, N Kopell, A Bibbig, E H Buhl, F E LeBeau, and M A Whittington. Gap junctions between interneuron dendrites can enhance synchrony of gamma oscillations in distributed networks. *J Neurosci*, 21(23):9478–9486, Dec 2001.

[28] Roger D Traub, Andreas Draguhn, Miles A Whittington, Torsten Baldeweg, Andrea Bibbig, Eberhard H Buhl, and Dietmar Schmitz. Axonal gap junctions between principal neurons: a novel source of network oscillations, and perhaps epileptogenesis. *Rev. Neurosci.*, 13(1):1–30, 2002.

[29] Roger D Traub, Roderick Duncan, Aline J C Russell, Torsten Baldeweg, Yuhai Tu, Mark O Cunningham, and Miles A Whittington. Spatiotemporal patterns of electrocorticographic very fast oscillations (¿ 80 hz) consistent with a network model based on electrical coupling between principal neurons. *Epilepsia*, 51(8):1587–1597, Aug 2010.

[30] M C van Rossum. A novel spike distance. *Neural Comput*, 13(4):751–763, Apr 2001.

[31] Yun Wang, Amey Barakat, and Hongwei Zhou. Electrotonic coupling between pyramidal neurons in the neocortex. *PLoS One*, 5(4):e10253, 2010.

[32] Yong-Chun Yu, Shuijin He, She Chen, Yinghui Fu, Keith N Brown, Xing-Hua Yao, Jian Ma, Kate P Gao, Gina E Sosinsky, Kun Huang, and Song-Hai Shi. Preferential electrical coupling regulates neocortical lineage-dependent microcircuit assembly. *Nature*, 486:113–7, 06 2012.

[33] Douglas Zhou, Aaditya V Rangan, David W McLaughlin, and David Cai. Spatiotemporal dynamics of neuronal population response in the primary visual cortex. *Proc Natl Acad Sci U S A*, 110(23):9517–9522, Jun 2013.

[34] Douglas Zhou, Yi Sun, Aaditya V Rangan, and David Cai. Spectrum of lyapunov exponents of non-smooth dynamical systems of integrate-and-fire type. *J Comput Neurosci*, 28(2):229–245, Apr 2010.

[35] S. Li, N. Liu, X. Zhang, D. W. McLaughlin, D. Zhou, and D. Cai. Dendritic computations captured by an effective point neuron model. *Proceedings of the National Academy of Sciences*, 116(30):15244–15252, 2019.